Research Article

Muhammad Shoaib, Faizan Ali, Muhammad Awais, Iqra Naz, Robicca Shamim, Kottakkaran Sooppy Nisar*, Muhammad Asif Zahoor Raja*, Muhammad Yousaf Malik, Mohamed Abbas, and C. Ahamed Saleel

Intelligent computing for the double-diffusive peristaltic rheology of magneto couple stress nanomaterials

https://doi.org/10.1515/ntrev-2022-0557 received January 15, 2023; accepted May 14, 2023

Abstract: In nanofluids, the effect of convection in the presence of double diffusivity on a magneto couple stress fluid with the peristaltic flow of a model in a non-uniform channel (MCSFM) is reviewed in this article. This research discusses MCSF in a non-uniform channel by applying the Levenberg–Marquardt procedure *via* an artificial backpro-

* Corresponding author: Kottakkaran Sooppy Nisar, Department of Mathematics, College of Science and Humanities, Prince Sattam Bin Abdulaziz University, Al Kharj, Saudi Arabia,

e-mail: n.sooppy@psau.edu.sa

* Corresponding author: Muhammad Asif Zahoor Raja, Future
Technology Research Center, National Yunlin University of Science and
Technology, 123 University Road, Section 3, Douliou, Yunlin 64002,
Taiwan, e-mail: rajamaz@yuntech.edu.tw

Muhammad Shoaib: Artificial Intelligence Center, Yuan Ze University, AI Center, Taoyuan 320, Taiwan

Faizan Ali: Department of Mathematics, COMSATS University Islamabad, Attock Campus, Attock 43600, Pakistan, e-mail: faziali1122@gmail.com Muhammad Awais: Department of Mathematics, COMSATS University Islamabad, Attock Campus, Attock 43600, Pakistan, e-mail: awais@ciit-attock.edu.pk

Iqra Naz: Department of Mathematics, COMSATS University Islamabad, Attock Campus, Attock 43600, Pakistan, e-mail: iqranaz617@gmail.com **Robicca Shamim:** Department of Mathematics, COMSATS University Islamabad, Attock Campus, Attock 43600, Pakistan, e-mail: robiccashamim234@gmail.com

Muhammad Yousaf Malik: Department of Mathematics, College of Sciences, King Khalid University, Abha, 61413, Saudi Arabia, e-mail: drmymalik@qau.edu.pk

Mohamed Abbas: Electrical Engineering Department, College of Engineering, King Khalid University, Abha 61421, Saudi Arabia, e-mail: mabas@kku.edu.sa

C. Ahamed Saleel: Department of Mechanical Engineering, College of Engineering, King Khalid University, Asir-Abha 61421, Saudi Arabia, e-mail: aveetil@kku.edu.sa

pagated neural network (LMP-ABNN). For two-dimensional and two-directional flows, mathematical formulations of double-diffusivity convection of a magneto couple stress fluid in nanofluids are developed. The partial differential equations are reduced to ordinary differential equations by using appropriate transformations. The assessment of the Hartmann number, thermophoresis parameter, Dufour parameter, Soret parameter, and magnetic Reynolds number over concentration profiles and temperature profiles is made by generating a dataset for LMP-ABNN based on the ND solve method for different variations of MSCFM. To examine the approximate solution validation, training and testing procedures are interpreted, and the performance is verified through error histogram and mean square error results. The extremely nonlinear equations are reduced by employing a long-wavelength approximation and a low but finite Reynolds number. To describe the behavior of flow quantities, graphical representations of a variety of physical characteristics of importance are shown. The impact of the Hartmann number and magnetic Reynolds number over axial magnetic field and current density is also studied. The concentration increases as the thermophoresis parameter and Dufour parameter values increase. This occurs because the concentration and both these parameters have a direct relationship. We observed opposite behavior for both the magnetic Reynolds number and the Hartman number. The behavior of current density I_z increases with increasing values of $R_{\rm m}$. Both the temperature distribution and solute concentration increase. The final outcome of this study is to provide the potential for these techniques to provide new insights and solutions to challenging problems in nanofluids and other areas of fluid mechanics and to facilitate the design of more efficient and effective microfluidic devices.

Keywords: double diffusivity, nanomaterial, peristalsis, nonuniform channel, low Reynolds number, induced magnetic field, couple stress fluid, backpropagation networks

Nomenclature

Α channel half-width at axial distance X В wave amplitude B_{C} volumetric solutal expansion \mathcal{C} propagation of velocity Csolute concentration $D_{\rm R}$ Brownian diffusion coefficient D_{S} solutal diffusivity D_{TC} **Dufour diffusivity** D_{T} thermophoretic diffusion coefficient $D_{\rm CT}$ Soret diffusivity Ε induced electric field G acceleration due to gravity thermal Grashof number G_{Rt} $G_{\rm rc}$ solutal Grashof number Grashof number for nanomaterials G_{Rf} current density I_z Le Lewis number $L_{\rm n}$ nanofluid Lewis number Hartmann number M Brownian motion parameter $N_{\rm R}$ **Dufour** parameter $N_{\rm TC}$ $N_{\rm t}$ thermophoresis parameter Soret parameter $N_{\rm CT}$ P pressure P_{r} Prandtl number sum of ordinary and magnetic pressures $p_{\rm m}$ Re Reynolds number magnetic Reynolds number $R_{\rm m}$ Stommer's number S_1 T time Τ temperature U, Vvelocity components in the Cartesian form α amplitude ratio θ dimensionless temperature electrical conductivity σ dimensionless solutal concentration Ω volume fraction of nanoparticles ψ stream function magnetic permeability $\mu_{\rm e}$ fluid density ρ_{f} mass density of nanoparticles $\rho_{\rm p}$ volumetric thermal expansion $\beta_{\rm T}$ thermal conductivity ς $(\rho c)_{\rm f}$ heat capacity of the fluid Θ volume fraction of nanoparticles μ viscosity of the fluid

half-width at the inlet

magnetic diffusivity

heat capacity of nanoparticles

 b_0

 $(\rho c)_{\rm p}$

 $\rho f_{\rm o}$ fluid density at $T_{\rm o}$ δ wave number

1 Introduction

A nanofluid, which consists of nano-sized particles suspended in liquid, has emerged as a promising candidate for heat transfer fluid design. Nanofluids are a novel type of nanotechnology-based heat transfer fluid. Nanofluids are created by distributing and stabilizing nanoparticles in conventional heat transfer fluids. Nanofluid technology could open up new avenues for developing nanotechnology-based coolants for a wide range of engineering and medicinal applications. As a result, nanofluid research has blossomed into a new field of scientific inquiry with cutting-edge applications. Also, nanofluids are a hot topic in both basic and practical research around the world. These fluids are employed in atomic reactors, hardware, and medical applications. The peristaltic mechanism is a fascinating phenomenon that has captivated the interest of many scientists due to its physiological and industrial uses. Peristalsis involving Newtonian and non-Newtonian fluids with various flow geometries has a significant range of literature. The urinary system, nutrient transportation in the intestinal system, reproductive tracts, and the female fallopian tube are all instances of peristaltic flows. Peristaltic flows are extensional flows since they comprise a sequence of propagating converging-diverging flows. As a consequence, in research studies of peristaltic flows, rheological models with good performance in extensional flows should be used. In 1966, Latham initiated the concept of the peristalsis mechanism and it was first observed and reported by Hardy and McDougall in 1894. In recent years, peristaltic movement research has gained popularity due to its importance in the transfer of liquids in biological systems.

A revolutionary wave of place expansion or contraction along the bendy channel dividers initiates this fluid motion mechanism. Peristalsis has recently attracted much interest from researchers. Since the innovative research of Latham [1] and Shapiro *et al.* [2], numerous experimental and theoretical initiatives on peristalsis have been made. Husseny *et al.* [3] analyzed the flow separation of peristaltic transport for Maxwell fluid between two coaxial tubes. The peristaltic motion of non-Newtonian fluids has been a major topic in chemical, biomedical, and environmental sciences and research recently. A great body of research has been conducted [4–9]. Stokes proposed the notion of the couple-stress fluid in 1966. Couple-stress fluid

is used in a variety of applications, including the scientific research of synovial joint lubrication mechanics. A human joint is a dynamically loaded bearing in which the bearing is articular cartilage and the lubricant is a synovial fluid. When a fluid is formed, squeeze-film action can significantly preserve the cartilage surface. The containing types of joints of the human body are the shoulder, ankle, knee, and hip joints. These joints provide low friction and very little erosion. The importance of non-Newtonian fluids was taken into consideration. This article explored thermal convection in a couple-stress fluid in the presence of a uniform vertical magnetic field and uniform rotation. The rotation has a stabilizing effect on stationary convection. Also, regulating and destructive effects are occurring due to magnetic field and couple stress. Kumar [10] studied the couple-stress fluid with magneto-rotatory thermal convection. Walicki and Walickia [11] analyzed the couplestress fluid in biological bearing with the inertia effects in the squeeze film. Sharma et al. [12] analyzed the behavior of suspended particles heated from below along with couple-stress fluid permeated. Hayat et al. [13] studied the influence of a magnetic field in the three-dimensional flow of couple-stress nanofluid over a nonlinearly stretching surface with convective conditions. Some efforts in this direction are mentioned here [14–21]. Conventional energy transfer is absolutely critical and occurs in a range of physical situations. Mixed convection has attracted greater attention than the other two forms of convection. When forced and free convections occur at the same time, this is known as mixed convection. Mixed convective energy transfer is investigated under various physical conditions and with various boundary limitations. Due to mixed convection, Prasad et al. [22] evaluated energy transfer in a horizontal tube filled with nanofluids. Among the important investigations on mixed convection energy transfer are the efforts of Hasnain et al. [23]. Yang et al. [24] have published a thorough investigation of the effective thermal conductivity of random hybrid polymers. Sharma et al. [25] used nanoparticles for peris non-Newtonian fluid peristaltic transfer to construct a mathematical model. The influence of nanofluids on peristaltic movement in an unequal channel was investigated by Khan et al. [26]. Khan [27] also proposed a two-issue four-equation nonhomogeneous equilibrium model for mass, momentum, and warmth transport in nanofluids. Bottemanne [28] investigated the natural boundary layer convection flow of a nanofluid. The influence of heat convection has been examined in various studies [29,30].

Artificial neural networks (ANNs) are inspired by the brain's diffuse, highly parallel computing, which allows it to perform so well at difficult navigation and recognition

tasks. Almost all artificial nodes are basic rational equations, in which variables are indeed the weighted combination of the node's data. Many numerical computing models have recently been put into practice in a wide range of fields, including nonlinear systems emerging in hydrodynamics [31,32], biomedical mathematics [33,34], and pantograph systems [35-37]. In second-grade fluid, an ANN is employed to study the physical aspects of heat generation [38], wire coating technique [39], and bioconvective flow model [40]. A robust ANN method called the backpropagation ANN model was able to establish ambiguous and nonlinear connections between the input biomarkers and the goal value by replicating complex processor neurons. The ANN successfully learns the association between model parameters and model parameters after numerous training sessions [41,42].

ANNs, genetic algorithms, and machine learning algorithms are examples of intelligent computing paradigms that can be used to examine the behavior of a Ree-Eyring fluid in a nanofluidic system [46]. The ohmic heating behavior and entropy generation of the system can be predicted by combining these intelligent computing paradigms with mathematical models of the nanofluidic system. This can aid in the design and improvement of nanofluidic systems for a range of uses, including the administration of drugs, the conversion of energy, and environmental cleanup. Raja et al. [47] examined entropy production (EP) of a magnetohydrodynamics viscous fluid flow model (MHD-VFFM) subject to a variable thickness surface with heat sink/source effect by utilizing the intelligent computing paradigm via artificial Levenberg-Marquardt backpropagated neural networks (ALM-BPNNs). Shoaib et al. [48] presented the Darcy-Forchheimer mixed convective flow model (DFMC-FM) by utilizing the algorithm of Levenberg Marquardt with backpropagated ANNs (ALM-BANN). In the study of Prasannakumar [49], a horizontal uniform magnetic field is used to regularize the flow field formed by a rotating disk. The horizontal magnetic field that is applied is not the same as the external upright magnetic field, and Bhatti et al. [51] investigated the peristaltically produced motion of pair stress fluid in the suspension of tiny particles. A non-uniform peristaltic wave is moving with a constant wave velocity. An electrically conducting, incompressible fluid with irrotational motion is subjected to an extrinsic magnetic field. Zeeshan et al. [52] centered on the mathematical study and modeling of some key aspects of these flows in a rectangular duct with wall characteristics. The effects of zeta potential, heat source, and Debye length are also investigated. Aqib et al. [53] analyzed the impact of heat transfer and magnetized Casson nanofluid flow on the boundary layer flow on a nonlinear stretchable surface.

Intelligent computing techniques have been widely used in fluid mechanics to simulate complex fluid dynamics and to predict fluid behavior in various applications. The double-diffusive peristaltic rheology of magneto couple stress nanomaterial is a particularly challenging problem due to the presence of multiple physical phenomena, such as diffusion, peristalsis, and magneto couple stress that interact with each other in a nonlinear and complex way.

Recent studies have explored the use of various intelligent computing techniques to model the double-diffusive peristaltic rheology of magneto couple stress nanomaterials, including ANNs, fuzzy logic, genetic algorithms, and particle swarm optimization. These techniques have been applied to various aspects of the problem, such as predicting the flow behavior, optimizing the design of microfluidic devices, and controlling the peristaltic flow. One recent study used a hybrid intelligent algorithm based on ANN and particle swarm optimization to simulate the peristaltic motion of magneto couple stress nanomaterials in a micro-channel. The model was able to accurately predict the flow characteristics and provided insights into the effect of different parameters on the flow behavior. Another study used a fuzzy logic-based model to optimize the design of a micro-channel for the peristaltic flow of magneto couple stress nanomaterials. The model was able to identify the optimal channel geometry for maximizing the pumping rate and minimizing the pressure drop.

The novelty of this research is the utilization of cutting-edge computational approaches to study and simulate the complex behavior of these materials in fluid dynamics, and it makes intelligent computing novel for the double-diffusive peristaltic rheology of magnetocoupling stress nanomaterial.

Double-diffusive convection, peristaltic motion, and magneto couple stress all occur together in nanomaterials to create a complex problem that is tricky to tackle using conventional analytical or numerical techniques. ANNs, fuzzy logic, and genetic algorithms are examples of intelligent computing methods that present a viable method for modeling and forecasting the behavior of these materials in intricate fluid systems.

These techniques can produce forecasts that are more precise and effective than those made using conventional techniques by utilizing the power of machine learning and optimization algorithms. They can also provide insights into the underlying physics of the system.

Moreover, the use of intelligent computing in this area of research is still a relatively new and emerging field, with many opportunities for further exploration and development. There is a potential for these techniques to provide new insights and solutions to challenging problems in

nanofluids and other areas of fluid mechanics and to facilitate the design of more efficient and effective microfluidic devices.

Classical fluid models are based on simplifying assumptions about fluid behavior that are often not accurate representations of the complex dynamics of real-world fluids. As such, they can be limited in their ability to accurately model certain phenomena. However, classical models are still widely used because they are relatively simple and computationally efficient and can provide useful approximations for a wide range of applications. New experimentally verified models, on the other hand, may incorporate more accurate representations of fluid dynamics and can potentially provide more accurate predictions for specific applications. However, these models can also be more complex and computationally intensive, which can make them less practical for certain types of simulations.

The important features of the authors of the study's innovative use of the LMP-ABNN integrated computational intelligence numerical solution:

- The worth and value of the suggested MCSFM were measured by analyzing the LMP-ABNN.
- The partial differential equations of MCSFM are converted into ordinary differential equations by applying some suitable similarity transformation.
- The ND-solve method is used to compute the dataset for the presented model.
- The error histogram, regression analysis, and mean square error plots are used to validate the performance of LMP-ABNN.

The rest of the study is organized in the following pattern: Section 2 gives a description of the model, Section 3 provides the solution of the model, Section 4 describes the results and discussion of the outcomes, and the last section gives the concluding remarks.

2 Description of the physical model

Considering a non-uniform tube with an electrically charged coupled stress fluid with the incompressible hydro-magnetic flow. The flow is created by waves traveling along the channel's walls.

We set an *X*-axis that is parallel in the parallel position that is adjusted for wave propagation. *Y*-axis is allocated a normal position when we compare it with wave propagation. Then, the mathematical expression is given as follows:

$$\hat{H}(h_X(X, Y, t), H_0 + h_Y(X, Y, t), 0).$$

The geometry of the wall surface is defined as

$$H(X, t) = a(X) + b \sin\left(\frac{2\pi}{\lambda}(X - ct)\right), \tag{1}$$

where $a(X) = b_0 + b_1 X$, in which b_0 represents the half-width and X represents the axial distance. The govern-

$$\frac{\partial V}{\partial Y} + \frac{\partial U}{\partial X} = 0, \tag{2}$$

$$\rho_{f} \left(U \frac{\partial}{\partial X} + \frac{\partial}{\partial t} + V \frac{\partial}{\partial Y} \right) U = -\frac{\partial P}{\partial X} + \mu \left[\frac{\partial^{2} U}{\partial X^{2}} + \frac{\partial^{2} U}{\partial Y^{2}} \right] - \eta \left[\frac{\partial^{4} U}{\partial X^{4}} + \frac{\partial^{4} U}{\partial Y^{4}} + 2 \frac{\partial^{4} U}{\partial X^{4} \partial Y^{4}} \right] - \frac{\mu_{e}}{2} \left[\frac{\partial H^{+2}}{\partial Y} \right] \\
+ \mu_{e} \left[h_{X} \frac{\partial h_{X}}{\partial X} + h_{Y} \frac{\partial h_{X}}{\partial Y} + H_{o} \frac{\partial h_{X}}{\partial Y} \right] + g\{ (1 - \Theta_{o}) \rho f_{o} \{ \beta_{T} (T - T_{o}) + \beta_{C} (C - C_{o}) \} \\
- (\rho_{p} - \rho f_{o}) (\Theta - \Theta_{o}) \}, \tag{3}$$

$$\rho_{f} \left(\frac{\partial}{\partial t} + U \frac{\partial}{\partial X} + V \frac{\partial}{\partial Y} \right) V = -\frac{\partial P}{\partial Y} + \mu \left(\frac{\partial^{2} V}{\partial X^{2}} + \frac{\partial^{2} V}{\partial Y^{2}} \right) - \eta \left(\frac{\partial^{4} V}{\partial X^{4}} + \frac{\partial^{4} V}{\partial Y^{4}} + 2 \frac{\partial^{4} V}{\partial X^{4} \partial Y^{4}} \right) - \frac{\mu_{e}}{2} \left(\frac{\partial H^{+2}}{\partial Y} \right) \\
+ \mu_{e} \left(h_{X} \frac{\partial h_{Y}}{\partial X} + h_{Y} \frac{\partial h_{Y}}{\partial Y} + H_{o} \frac{\partial h_{Y}}{\partial Y} \right) + g \{ (1 - \Theta_{o}) \rho f_{o} \{ \beta_{T} (T - T_{o}) + \beta_{C} (C - C_{o}) \} \\
- (\rho_{p} - \rho f_{o}) (\Theta - \Theta_{o}) \}, \tag{4}$$

$$(\rho c)_{f} \left[U \frac{\partial}{\partial X} + \frac{\partial}{\partial t} + V \frac{\partial}{\partial Y} \right] T = \sigma \left[\frac{\partial^{2} T}{\partial X^{2}} + \frac{\partial^{2} T}{\partial Y^{2}} \right] + (\rho c)_{p} \left[D_{B} \left(\frac{\partial \Theta}{\partial X} \frac{\partial T}{\partial X} + \frac{\partial \Theta}{\partial Y} \frac{\partial T}{\partial Y} \right) \left(\frac{D_{T}}{T_{o}} \right) \left[\left(\frac{\partial T}{\partial X} \right)^{2} + \left(\frac{\partial T}{\partial Y} \right)^{2} \right] \right] + D_{TC} \left(\frac{\partial^{2} C}{\partial X^{2}} + \frac{\partial^{2} C}{\partial Y^{2}} \right),$$
(5)

$$\left(\frac{\partial}{\partial t} + U \frac{\partial}{\partial X} + V \frac{\partial}{\partial Y}\right) \Theta = D_{\rm B} \left(\frac{\partial^2 \Theta}{\partial X^2} + \frac{\partial^2 \Theta}{\partial Y^2}\right) + \left(\frac{D_T}{T_0}\right) \left(\frac{\partial^2 T}{\partial X^2} + \frac{\partial^2 T}{\partial Y^2}\right). \tag{6}$$

In the laboratory, the flow is unsteady, but in the wave frame, it is steady, associated as

$$x = X - ct$$
, $u = U - c$, $y = Y$, $v = V$, and $p(x, y) = P(X, Y, t)$, (7)

where c denotes the velocity gradient, and U and V are the velocity components in a Cartesian form.

2.1 Similarity transformations

Using the following transformations,

$$\bar{x} = \frac{x}{\lambda}, \quad \bar{y} = \frac{y}{b_{0}}, \quad \bar{v} = \frac{v}{c}, \quad \bar{u} = \frac{u}{c}, \quad \delta = \frac{b_{0}}{\lambda}, \quad \bar{p} = \frac{b_{0}^{2}p}{\mu c \lambda}, \quad \bar{t} = \frac{ct}{\lambda}, \quad M^{2} = R_{e}R_{m}S_{1}^{2}, \quad R_{e} = \frac{\rho_{f}cb_{o}}{\mu}, \quad \theta = \frac{T - T_{o}}{T_{1} - T_{o}}, \\
R_{m} = \sigma\mu_{e}b_{o}c, \quad S_{1} = \frac{H_{o}}{c}\sqrt{\frac{\mu_{e}}{\rho}}, \quad \bar{h} = \frac{h}{b_{o}}, \quad \Phi = \frac{\Phi}{H_{o}b_{o}}, \quad \gamma = \frac{C - C_{o}}{C_{1} - C_{o}}, \quad P_{r} = \frac{(\rho c)_{f}v}{\sigma}, \quad p_{m} = p + \frac{1}{2}R_{e}\delta\frac{\mu_{e}(H^{+})^{2}}{\rho_{f}c^{2}}, \\
\Omega = \frac{\Theta - \Theta_{o}}{\Theta_{1} - \Theta_{o}}, \quad L_{n} = \frac{v}{D_{B}}, \quad L_{e} = \frac{v}{D_{S}}, \quad N_{CT} = \frac{D_{CT}(T_{1} - T_{o})}{(C_{1} - C_{o})D_{S}}, \quad N_{TC} = \frac{D_{CT}(C_{1} - C_{o})}{\sigma(T_{1} - T_{o})}, \quad K = \sqrt{\frac{\mu}{\eta}}b_{o}, \quad N_{b} = \frac{(\rho c)_{p}D_{B}(\Theta_{1} - \Theta_{o})}{\sigma}, \\
N_{t} = \frac{(\rho c)_{p}D_{T}(T_{1} - T_{o})}{T_{o}\sigma}, \quad G_{rF} = \frac{g(\rho_{p} - \rho_{f})(\Theta_{1} - \Theta_{o})}{\mu_{o}c}b_{o}^{2}, \quad G_{rc} = \frac{g(1 - \Theta_{o})\rho_{f}\beta_{c}(C_{1} - C_{o})b_{o}^{2}}{\mu_{o}c}, \quad \nabla^{2} = \delta^{2}\frac{\partial^{2}}{\partial x^{2}} + \frac{\partial^{2}}{\partial y^{2}}, \\
u = \frac{\partial\psi}{\partial y}, \quad v = -\delta\frac{\partial\psi}{\partial x}, \quad h_{x} = \frac{\partial\Phi}{\partial y}, \quad h_{y} = -\delta\frac{\partial\Phi}{\partial x}.$$

Using equations (7) and (8), equations (1-6) become

$$R_{\rm e}\delta(\psi_y\psi_{xy}-\psi_x\psi_{yy}) = -\frac{\partial p_{\rm m}}{\partial x} + \nabla^2\psi_y - \frac{1}{k^2}\nabla^4\psi_y + R_{\rm e}S_1^2\Phi_{yy} + R_{\rm e}S_1^2\delta(\Phi_y\Phi_{xy}-\Phi_x\Phi_{yy}) + G_{\rm rt}\theta + G_{\rm rc}\gamma - G_{\rm rF}\Omega, \tag{9}$$

$$R_{\rm e}\delta^{3}(\psi_{x}\psi_{xy} - \psi_{y}\psi_{xx}) = -\frac{\partial p_{\rm m}}{\partial y} + \delta^{2}\nabla^{2}\psi_{x} + \frac{\delta^{2}}{k^{2}}\nabla^{4}\psi_{x}$$

$$- R_{\rm e}\delta^{2}S_{1}^{2}\Phi_{yy} \qquad (10)$$

$$- R_{\rm e}S_{1}^{2}\delta^{3}(\Phi_{y}\Phi_{xx} - \Phi_{x}\Phi_{xy})$$

$$+ \delta(G_{\rm rt}\theta + G_{\rm rc}\gamma - G_{\rm rF}\Omega),$$

$$R_{e}P_{r}\delta(\psi_{y}\theta_{x} - \psi_{x}\theta_{y}) = (\theta_{yy} + \delta^{2}\theta_{xx}) + N_{TC}(\delta^{2}\gamma_{xx} + \gamma_{yy})$$

$$+ N_{b}(\delta^{2}\theta_{x}\Omega_{x} + \theta_{y}\Omega_{y})$$

$$+ N_{t}(\delta^{2}(\theta_{x})^{2} + (\theta_{y})^{2}),$$

$$(11)$$

$$R_{\rm e}\delta L_{\rm e}(\psi_y\gamma_x-\psi_x\gamma_y)=(\gamma_{yy}+\delta^2\gamma_{xx})+N_{\rm CT}(\delta^2\theta_{xx}+\theta_{yy}), \eqno(12)$$

$$\begin{split} R_{\rm e}\delta L_{\rm n}(\psi_y \Omega_x - \psi_x \Omega_y) &= (\Omega_{yy} + \delta^2 \Omega_{xx}) \\ &+ \frac{N_{\rm t}}{N_{\rm B}} (\delta^2 \theta_{xx} + \theta_{yy}), \end{split} \tag{13}$$

$$\psi_{y} - \delta(\psi_{y}\Phi_{x} - \psi_{x}\phi_{y}) + \frac{1}{R_{m}}(\Phi_{yy} + \delta^{2}\Phi_{xx}) = E. \quad (14)$$

Equations (9)–(14) were simplified to the following form after using the low but finite Reynolds and long wavelength:

$$-\frac{\partial p}{\partial x} + \frac{\partial^3 \psi}{\partial y^3} - \frac{1}{k^2} \frac{\partial^5 \psi}{\partial y^5} + R_e S_1^2 \Phi_{yy} + G_{rt} \theta + G_{rc} \gamma$$

$$-G_{rr} \Omega = 0,$$
(15)

$$-\frac{\partial p}{\partial v} = 0,\tag{16}$$

$$\frac{\partial^{2} \theta}{\partial y^{2}} + N_{TC} \frac{\partial^{2} y}{\partial y^{2}} + N_{B} \left(\frac{\partial \theta}{\partial y} \frac{\partial \Omega}{\partial y} \right) + N_{t} \left(\frac{\partial \theta}{\partial y} \right)^{2} + 0, \quad (17)$$

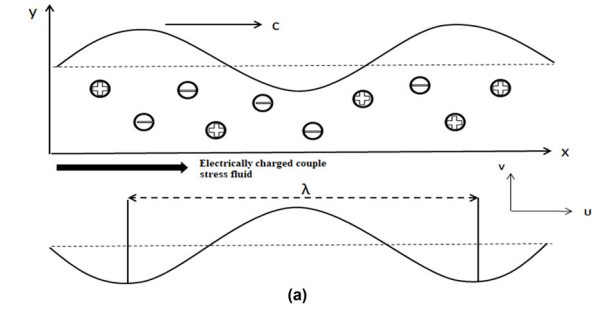
$$\frac{\partial^2 \gamma}{\partial y^2} + N_{\rm CT} \frac{\partial^2 \theta}{\partial y^2} = 0, \tag{18}$$

$$\frac{\partial^2 \Omega}{\partial v^2} + \frac{N_t}{N_c} \frac{\partial^2 \theta}{\partial v^2} = 0, \tag{19}$$

$$\Phi_{yy} = R_{\rm m}(E - \psi_{\rm v}). \tag{20}$$

3 Solution methodology

The partial differential equations are converted into ordinary differential equations by applying similarity transformation, which is suitable for MCSFM then we apply the ND-solve method to solve the ODEs and obtain the reference dataset for LMP-ABNN. This reference dataset is utilized in Matlab and computed for different scenarios of MCSFM by varying the values of different parameters, *i.e.*, Hartmann number, thermophoresis parameter, Dufour parameter, Soret parameter, and magnetic Reynolds number. The reference dataset is generated for 101 input points, of which there are 80% points for training, 10% for testing, and 10% for validation. The neural network diagram is given in Figure 1(b). The sketch of the neural network for the fluid flow system is depicted in Figure 1(b) in terms of input structure, *i.e.*, a vector



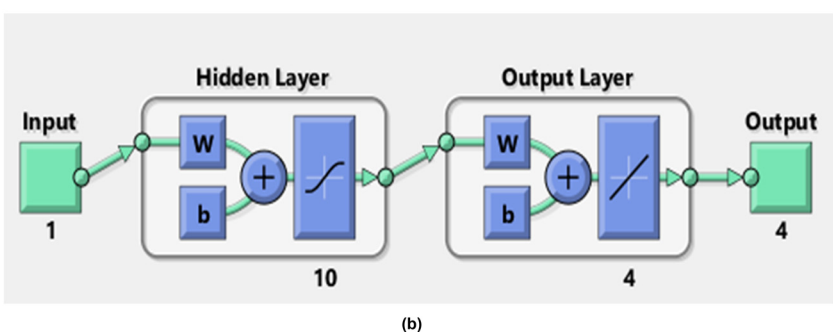


Figure 1: (a) Flow geometry and (b) neural network for the magneto couple stress fluid model.

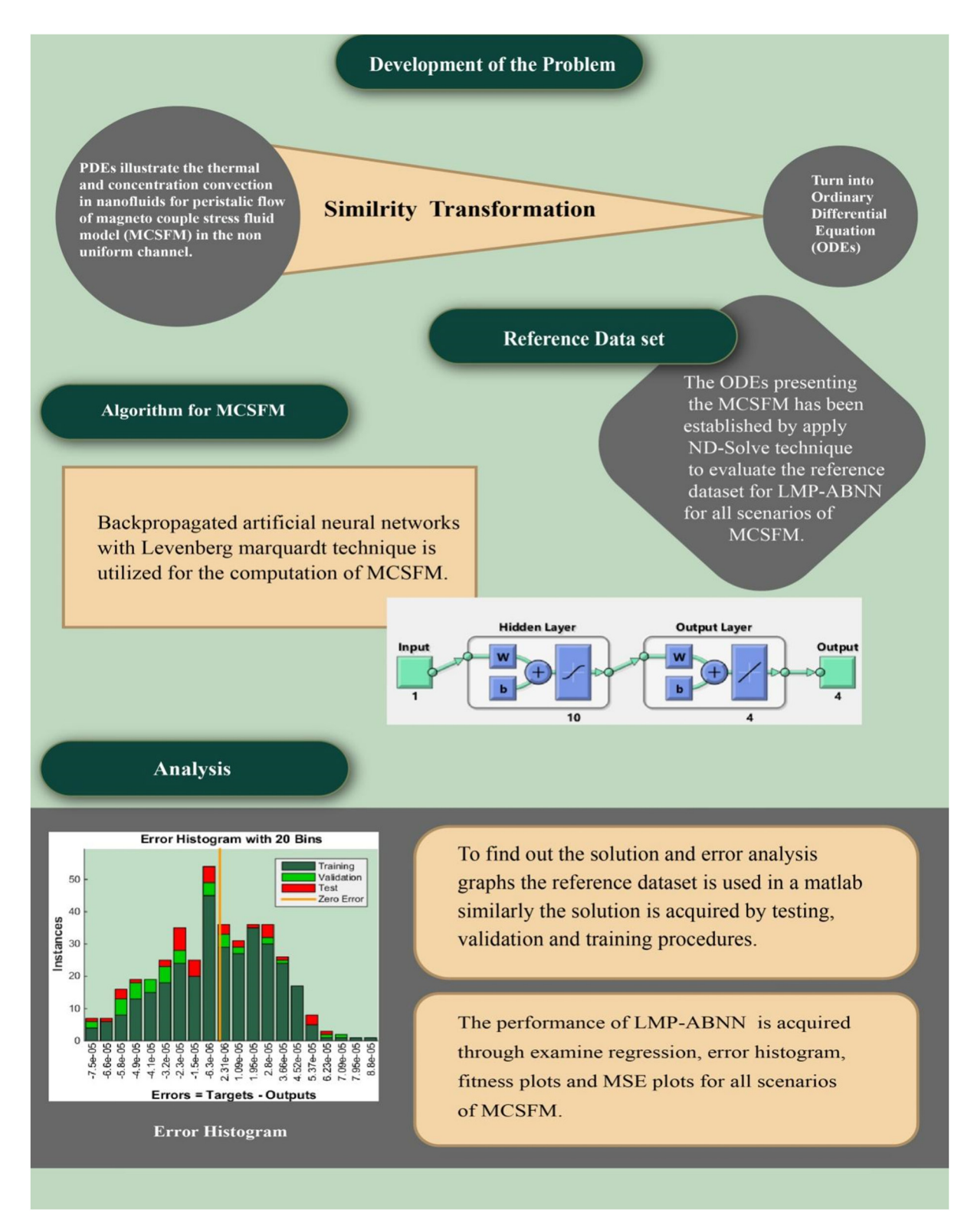


Figure 2: Flow chart of the magneto couple stress fluid model.

representing the input grid points, hidden layer exploiting 10 hidden neurons with log-sigmoidal activation function, i.e., f(x) = (1 + e - x) - 1, and the output layer with a matrix of approximate solutions, while a linear activation function is used here, *i.e.*, f(x) = x. Moreover, Figure 1(b) illustrates a single neural network model. The purpose of the activation function,

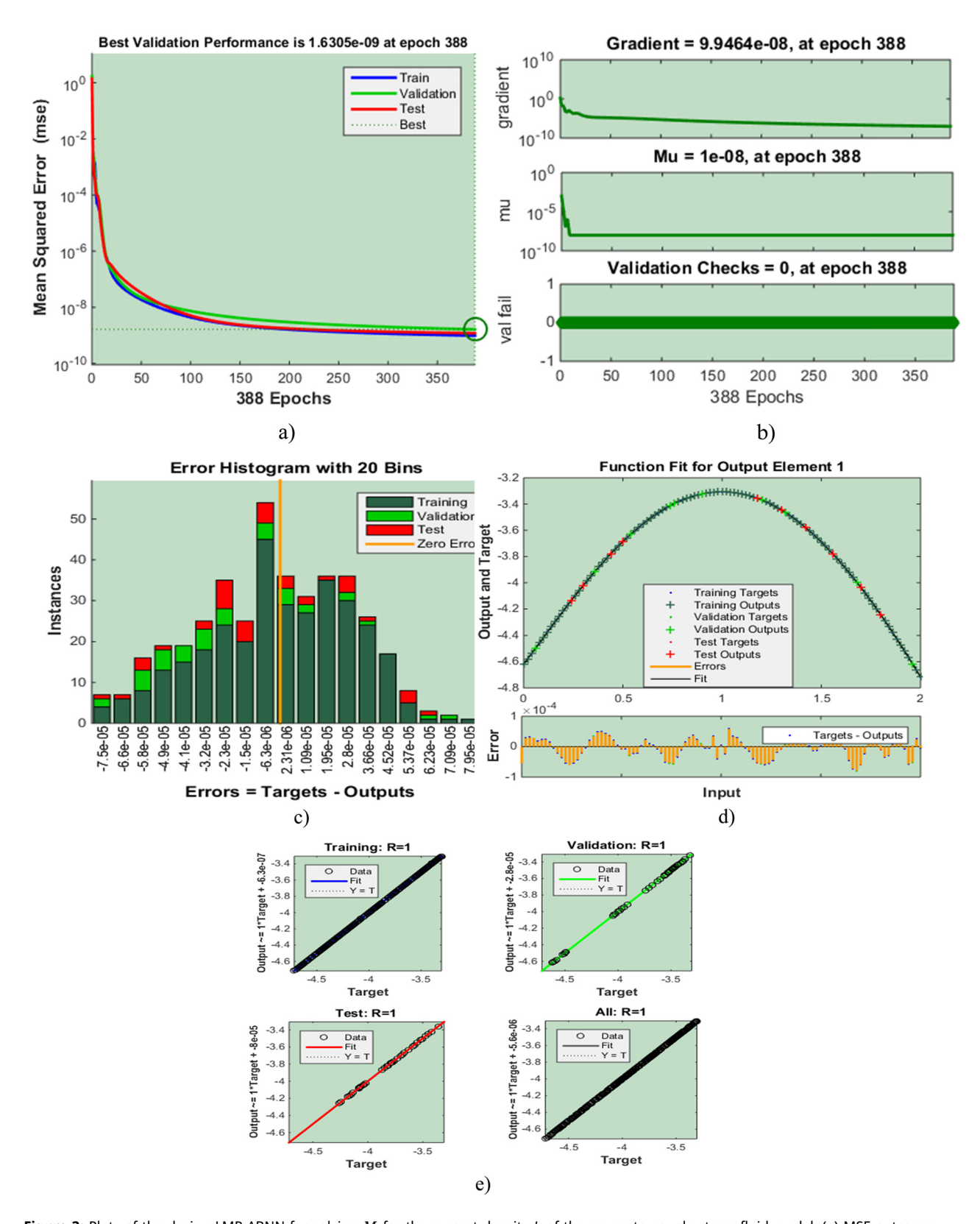


Figure 3: Plots of the design LMP-ABNN for solving M for the current density J_z of the magneto couple stress fluid model: (a) MSE outcomes, (b) transition state, (c) error histogram, (d) fitting curve, and (e) regression.

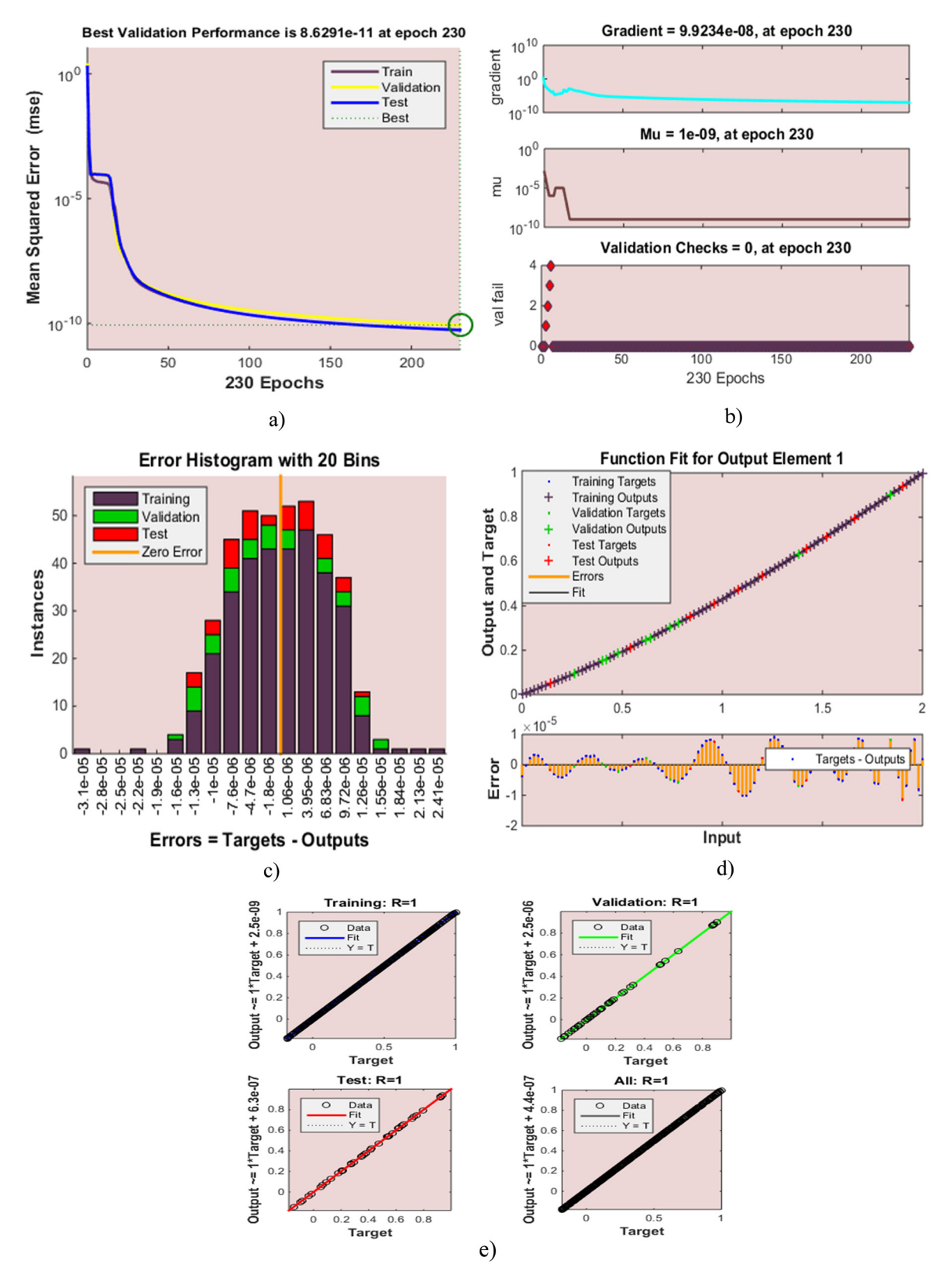


Figure 4: Plots of the design LMP-ABNN for solving N_t for λ of the magneto couple stress fluid model: (a) MSE outcomes, (b) transition state, (c) error histogram, (d) fitting curve, and (e) regression.

used in each layer of neural networking, is to induce nonlinearity into a neuron's output. Because the gradients are given simultaneously with the inaccuracy to modify the weights and biases, activation functions enable backpropagation. The activation function transforms the data in a nonlinear way, allowing it to understand and accomplish increasingly complicated operations.

Figure 3 presents the graphs of performance, training, transition state, error histogram, and regression for the design LMP-ABNN for solving the Hartmann number (M) for the current density (J_z). Figure 4 describes the plots of the design LMP-ABNN for solving the thermophoresis

Table 1: Values of all variants of MCSFM

Scenarios	Cases	Physical quantities					
		М	N _t	N _{TC}	N _{CT}	<i>R</i> _m	
1	1	0.1	6	6	1	2	
	2	0.7	6	6	1	2	
	3	1.5	6	6	1	2	
	4	1.7	6	6	1	2	
2	1	0.1	0.0	0.6	0.6	2	
	2	0.1	1.5	0.6	0.6	2	
	3	0.1	3.0	0.6	0.6	2	
	4	0.1	4.5	0.6	0.6	2	
3	1	0.1	0.6	0.0	0.6	2	
	2	0.1	0.6	0.5	0.6	2	
	3	0.1	0.6	1.0	0.6	2	
	4	0.1	0.6	1.5	0.6	2	
4	1	0.1	0.6	0.6	0.0	2	
	2	0.1	0.6	0.6	0.5	2	
	3	0.1	0.6	0.6	1.0	2	
	4	0.1	0.6	0.6	1.5	2	
5	1	0.1	0.6	0.6	0	1.0	
	2	0.1	0.6	0.6	0	2.0	
	3	0.1	0.6	0.6	0	3.0	
	4	0.1	0.6	0.6	0	4.0	
6	1	0.1	0.0	0.5	0.5	2	
	2	0.1	0.5	0.5	0.5	2	
	3	0.1	1.0	0.5	0.5	2	
	4	0.1	1.5	0.5	0.5	2	

parameter $N_{\rm t}$ and Dufour parameter $N_{\rm TC}$ for the concentration profile λ . Similarly, the plots for the design LMP-ABNN for solving $N_{\rm TC}$ for Ω are shown in Figures 6 and 7 shows the plots of the design LMP-ABNN of $R_{\rm m}$ for induced magnetic field $h_{\rm x}$. Figure 8 describes the plots of the design LMP-ABNN for solving $N_{\rm t}$ for the temperature profile θ of MCSFM. Table 1 describes the values of all variants of MCSFM, and Table 2 describes the outcomes of all varying parameters of LMP-ABNN. In this article, six scenarios are discussed for different cases of MCSFM. The Hartmann number (M), thermophoresis parameter $(N_{\rm t})$, Dufour parameter $N_{\rm TC}$, Soret parameter $N_{\rm CT}$, and magnetic Reynolds number $(R_{\rm m})$ are described in Table 1. There are ten hidden neurons, and the flow chart of the presented model is shown in Figure 2.

4 Results and discussion

Figure 3(a)–(e) shows the MSE variation, state transition outcomes, error histogram plots, regression analysis, and comparison of ANNs-BRS with reference solution for the magnetic parameter M of case 4. Similarly, Figures 4(a)–(e), 5(a)–(e), and 6(a)–(e) characterize the variation of mean square error, state transition outcomes, plots of error histogram, regression demonstration, and comparison of ANNs-BRS with the reference outcome for the thermophoresis parameter $N_{\rm t}$, Dufour parameter $N_{\rm TC}$, and Soret parameter $N_{\rm CT.}$ respectively. From Figure 3(a) and (b), it is found that the best training performance is 1.6305×10^{-9} at epoch 388, having a gradient value of 9.9464×10^{-8} and Mu of 1×10^{-8} at epoch 388. A plot of the error histogram is presented in Figure 3(c). The ANNs-BRS outcome comparison with the reference solution is presented in Figure 3(d), which shows a close agreement between the reference solution and ANNs-BRS having an MSE error in the range of 10^{-12} , which proves the validity of the proposed scheme. The regression plot for the current density I_z is presented in Figure 3(e). From Figures 4(a), 5(a), 6(a), 7(a), and 8(a),

Table 2: Outcomes of all cases

Physical quantities	Distribution	MSE training	Validation	Testing	Performance	Grad	Mu	Epochs	Time (s)
M	J_{z}	9.79 × 10 ⁻¹⁰	1.63 × 10 ⁻⁹	1.19 × 10 ⁻⁹	9.80 × 10 ⁻¹⁰	9.95 × 10 ⁻⁸	1.00 × 10 ⁻⁸	388	59
N_{t}	λ	5.43×10^{-11}	8.62×10^{-11}	5.47×10^{-11}	5.43×10^{-11}	9.92×10^{-8}	1.00×10^{-9}	230	43
N_{TC}	λ	7.84×10^{-10}	1.28×10^{-9}	1.31×10^{-9}	7.85×10^{-10}	9.92×10^{-8}	1.00×10^{-8}	312	4
N _{CT}	Ω	2.88×10^{-10}	5.54×10^{-10}	4.89×10^{-10}	2.89×10^{-10}	1.58×10^{-7}	1.00×10^{-8}	1,000	15
R _m	hx	3.78×10^{-10}	6.55×10^{-10}	6.19×10^{-10}	3.79 × 10 ⁻ 10	2.48×10^{-7}	1.00×10^{-8}	1,000	15
N_{t}	θ	6.85×10^{-10}	8.28×10^{-10}	9.62×10^{-10}	6.86×10^{-10}	9.90×10^{-8}	1.00×10^{-8}	189	3

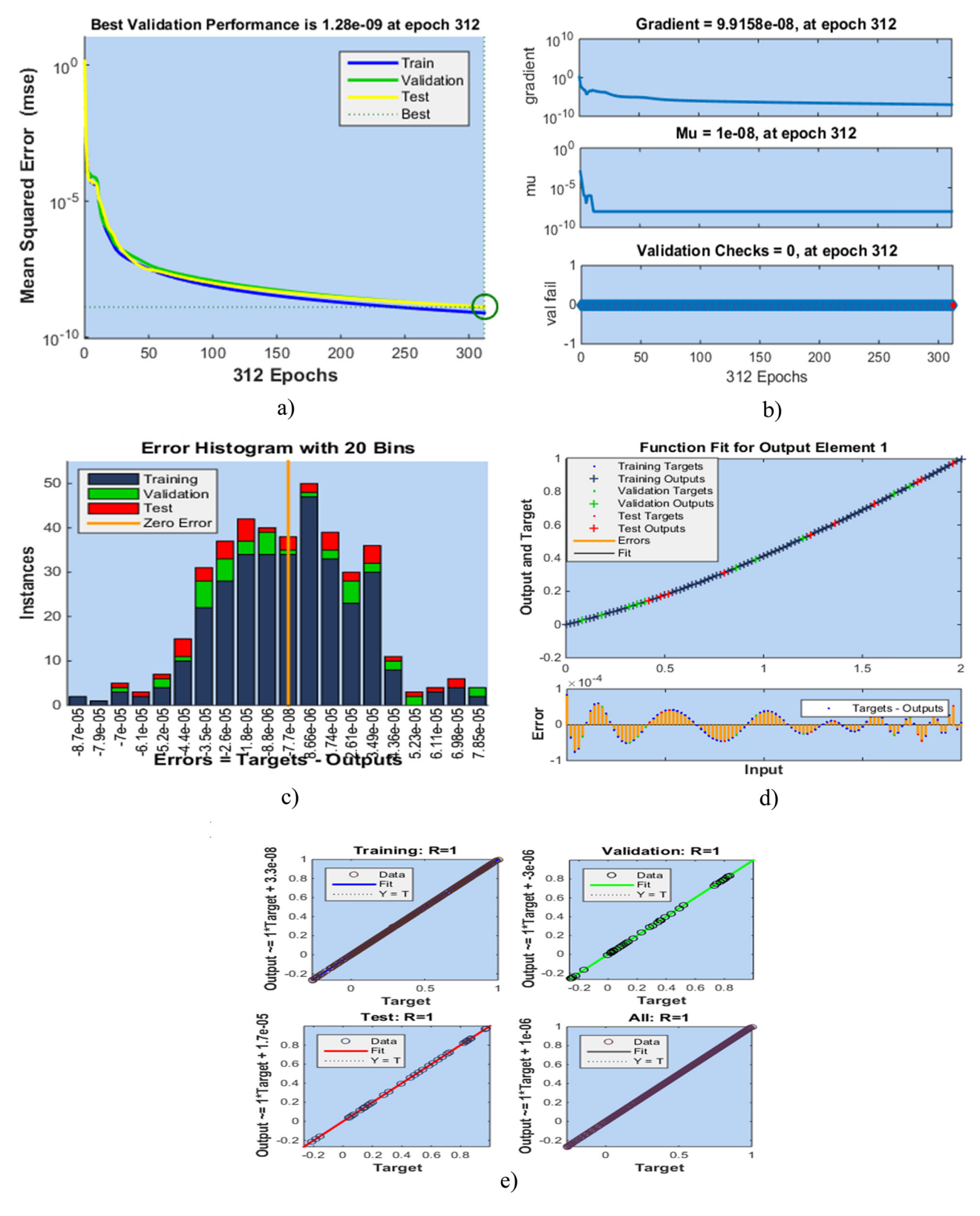


Figure 5: Plots of the design LMP-ABNN for solving N_{TC} for λ of the magneto couple stress fluid model: (a) MSE outcomes, (b) transition state, (c) error histogram, (d) fitting curve, and (e) regression.

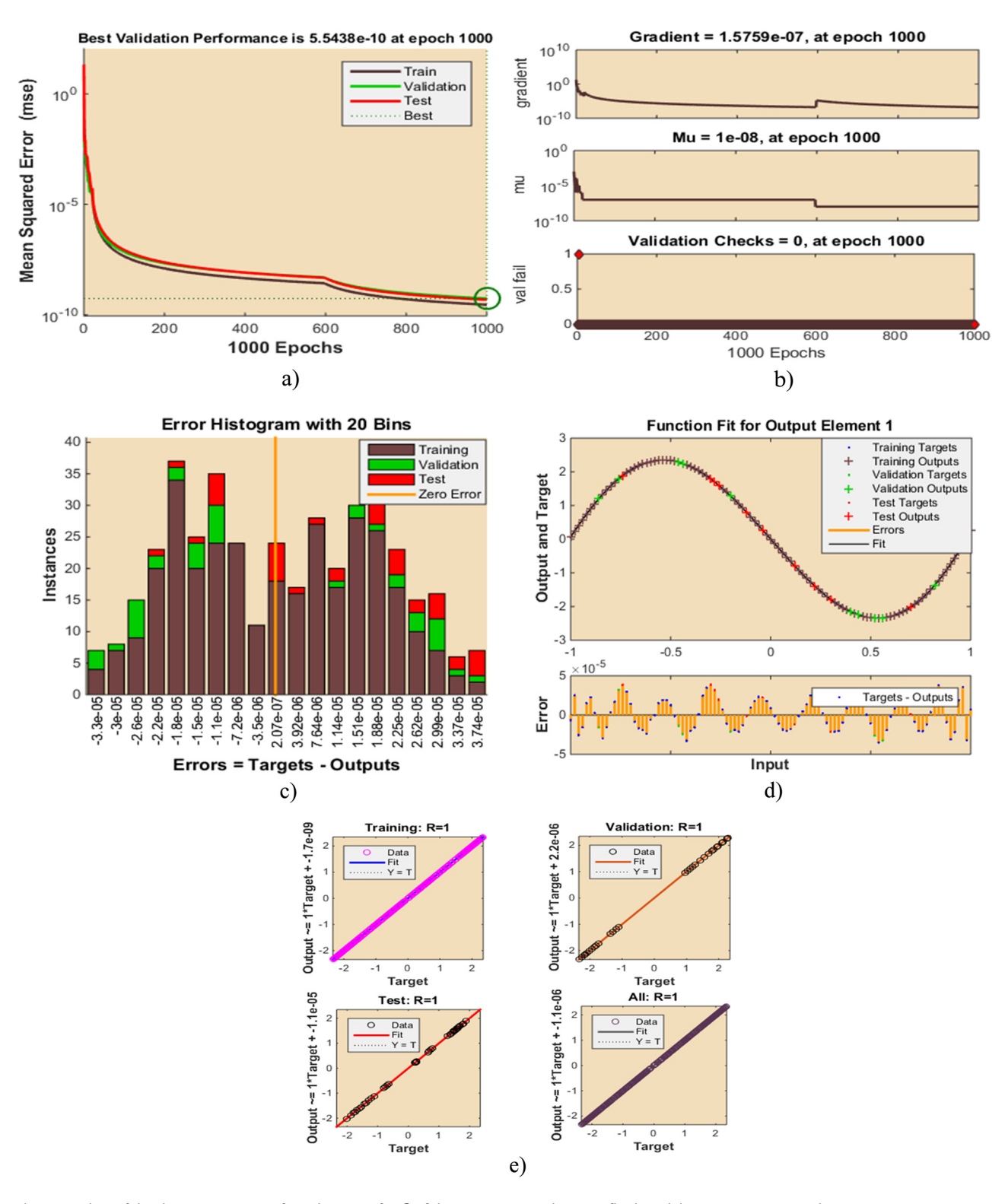


Figure 6: Plots of the design LMP-ABNN for solving N_{CT} for Ω of the magneto couple stress fluid model. (a) MSE outcomes, (b) transition state, (c) error histogram, (d) fitting curve, and (e) regression.

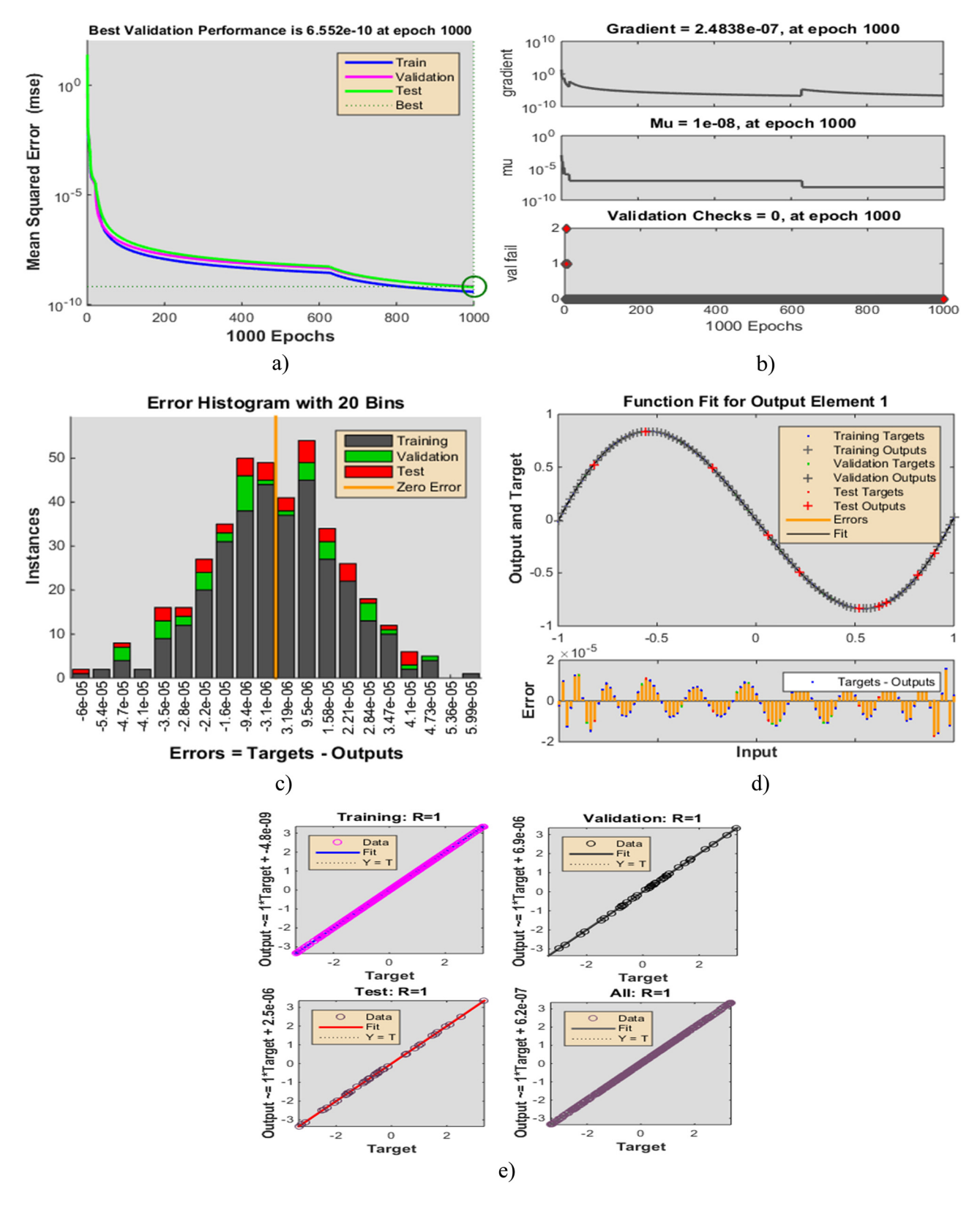


Figure 7: Plots of the design LMP-ABNN for solving $R_{\rm m}$ for $h_{\rm x}$ for the magneto couple stress fluid model: (a) MSE outcomes, (b) transition state, (c) error histogram, (d) fitting curve, and (e) regression.

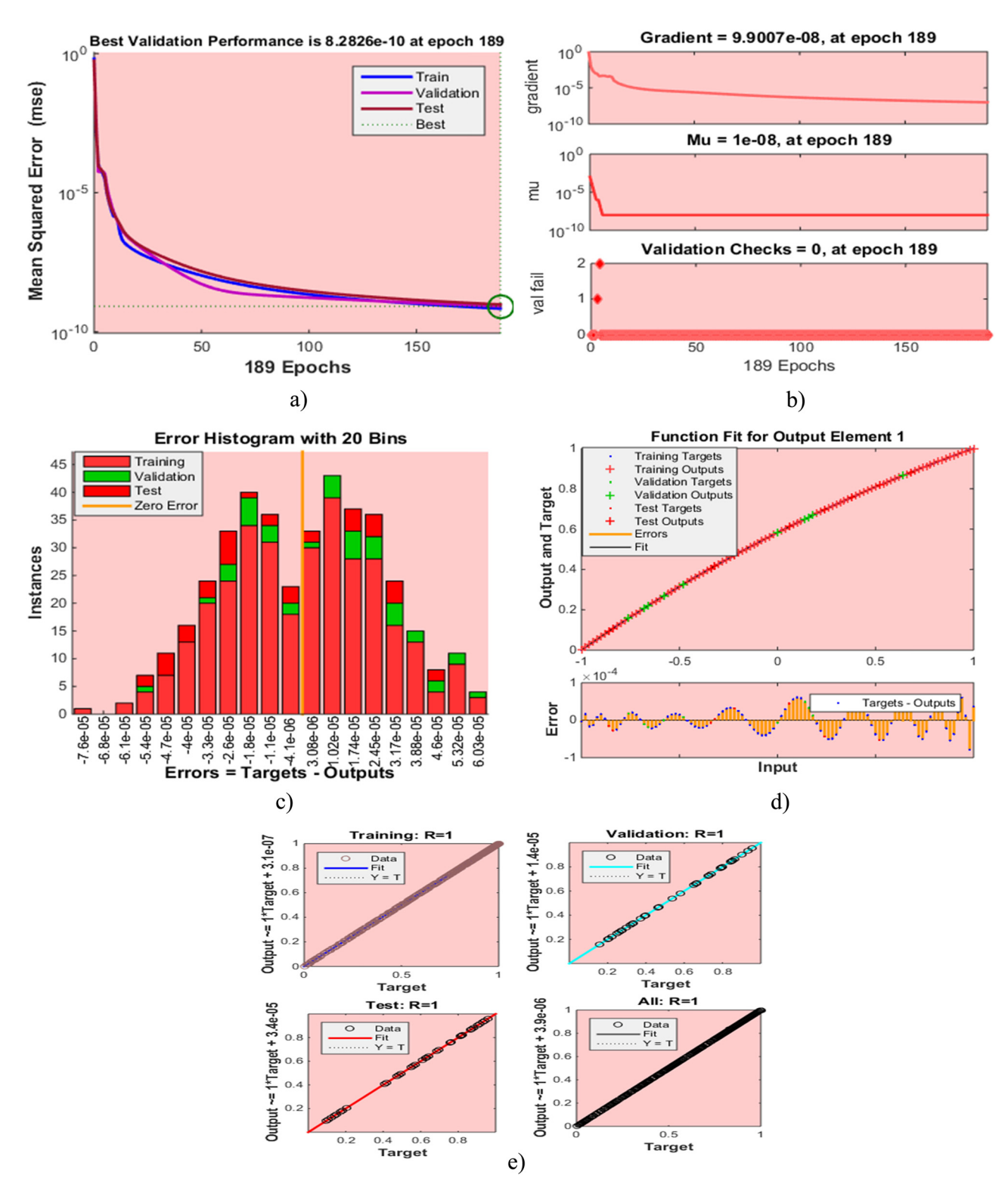


Figure 8: Plots of the design LMP-ABNN for solving N_t for θ of the magneto couple stress fluid model: (a) MSE outcomes, (b) transition state, (c) error histogram, (d) fitting curve, and (e) regression.

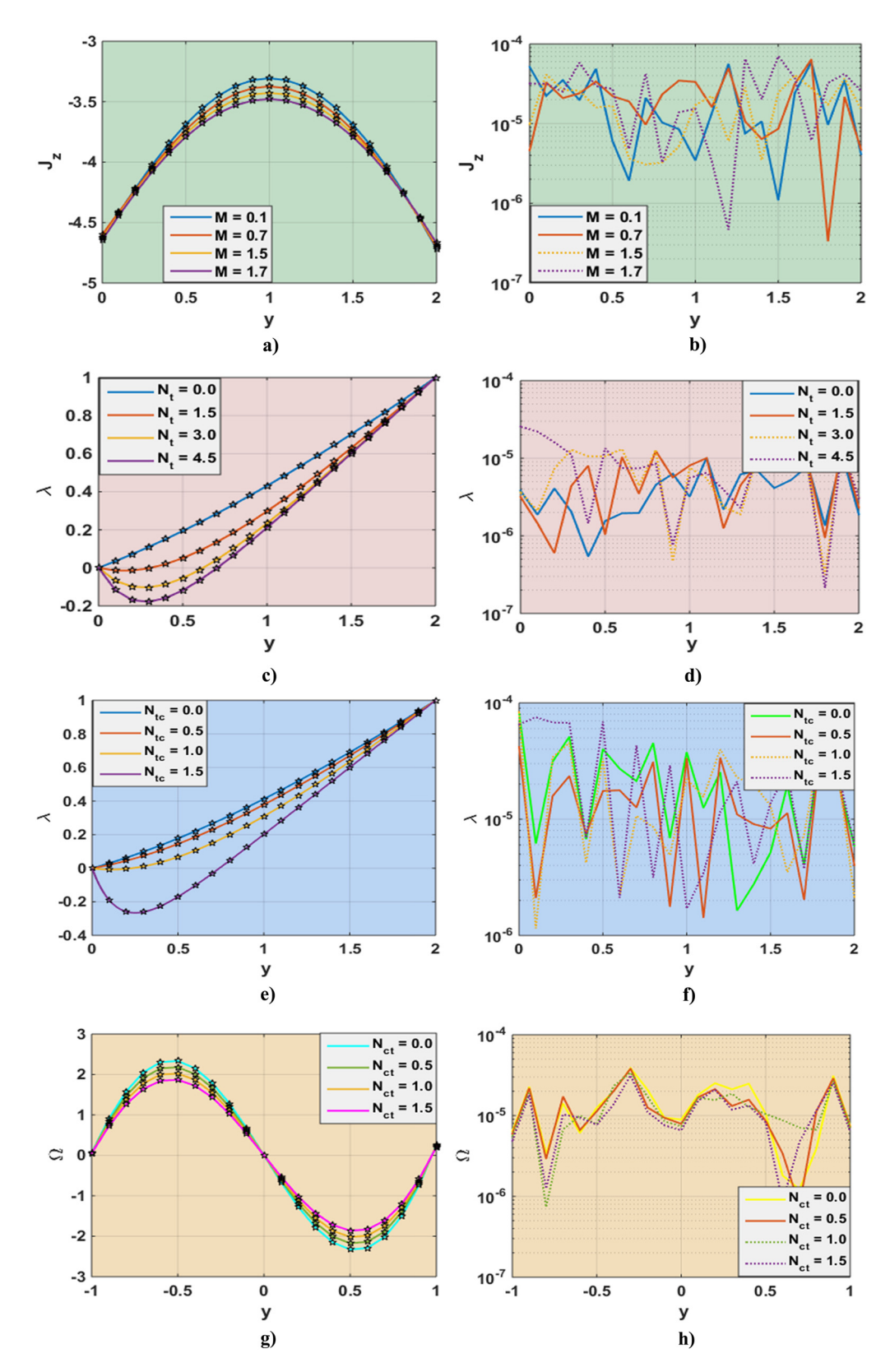


Figure 9: Solution and error plots of LMP-ABNN for J_z , λ , Ω , h_x , and θ with the reference dataset of the magneto couple stress fluid model. (a) Impact of M on J_z , (b) analysis of absolute errors, (c) impact of N_t on λ , (d) analysis of absolute errors, (e) impact of N_t on λ , (f) analysis of absolute errors, (g) impact of N_t on Ω , (h) analysis of absolute errors, (i) variation of R_m for h_x , (j) absolute error analysis, (k) variation of N_t for θ , and (l) absolute error analysis.

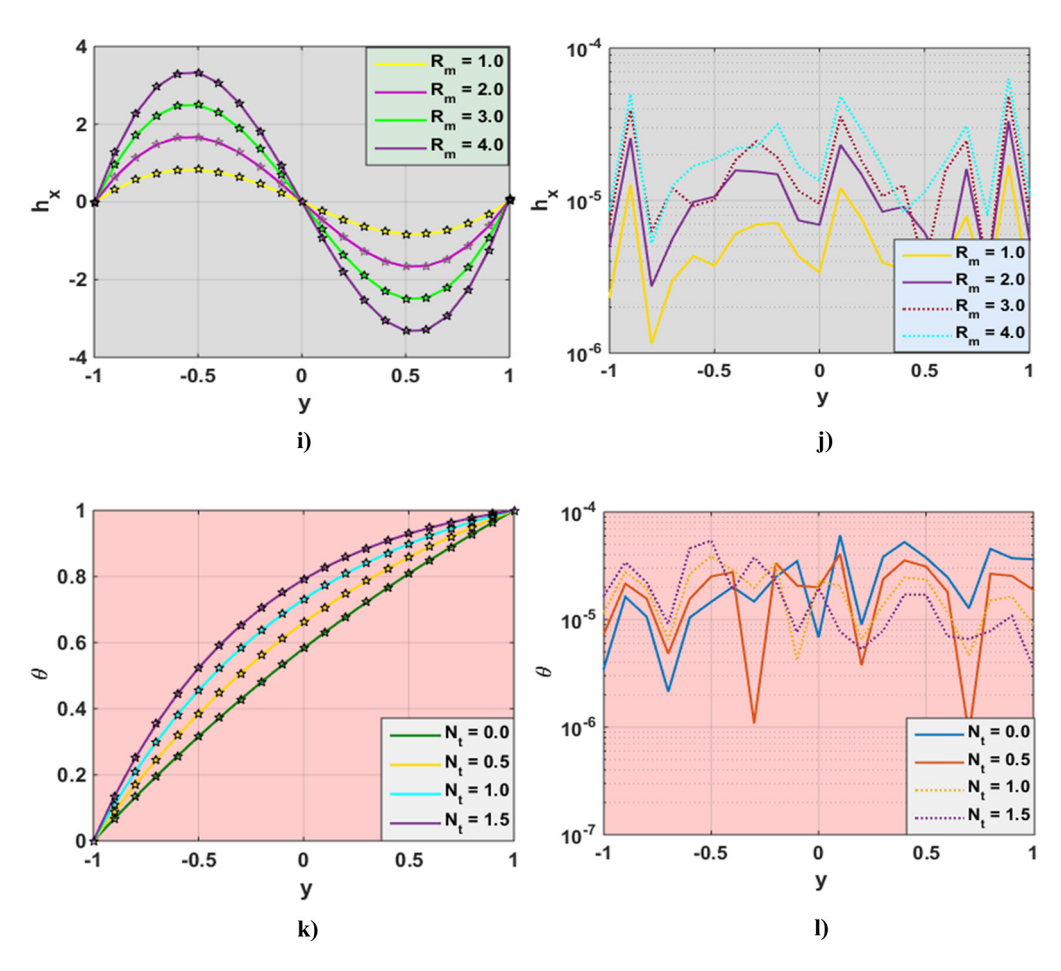


Figure 9: (Continued)

it can be observed that the best training performances are 8.6291×10^{-11} , 1.28×10^{-9} , 5.5438×10^{-10} , 6.652×10^{-10} , and 8.2826×10^{-10} at epochs 230, 312, 1,000, 1,000, and 189 for solving $N_{\rm t}$ for λ , for solving $N_{\rm TC}$ for λ , for solving $N_{\rm CT}$ for Ω , for solving $R_{\rm m}$ for $h_{\rm x}$, and for solving $N_{\rm t}$ for θ , respectively. One may notice from these figures that the trained data are validated very accurately for all scenarios. Figures 4(b), 5(b), 6(b), 7(b), and 8(b) present the outcomes of state transition describing gradient values and epoch numbers along with validation checks for various scenarios. From these figures, one may observe that the gradient values are $3.94 \times$ 10^{-8} , 6.089 × 10^{-8} and 9.133 × 10^{-8} , and Mu values are 1 × 10⁻⁸ for each scenario, at epochs 312, 1,000, 1,000 and 189 for solving the Dufour parameter for λ , Soret parameter for Ω , $R_{\rm m}$ for $h_{\rm x}$, and $N_{\rm t}$ for θ , respectively. The plots of error histograms are presented in Figures 3(c), 4(c), 5(c), 6(c) and 7(c) for the current density I_z , N_t for λ , N_{TC} for λ , $N_{\rm CT}$ for Ω , and $R_{\rm m}$ for $h_{\rm x}$, respectively. It is found from these plots that the error between the target and output is almost approaching zero. The regression graphs for $N_{\rm CT}$ for Ω , $R_{\rm m}$

for h_x , and N_t for θ are shown in Figures 6(e), 7(e), and 8(e), respectively. The smaller values of MSE depict a more reliable solution and regression plots calculate the correlation between outputs and targets; if R is close to 1, it indicates a close relationship; while if R is close to 0, it represents a random relationship. Comparison plots of ANNs-BRS with the reference solution for all scenarios are plotted in Figures 6(e), 7(e), and 8(e).

Figure 9(a) and (l) describes the solution and error analysis plots of LMP-ABNN for all scenarios of MCSFM. We observed that the behavior of solutal concentration is increasing by increasing the parameters $N_{\rm t}$ and $N_{\rm TC}$ shown in Figures 9(c) and (e) because the solutal concentration has a direct relation with $N_{\rm t}$ and $N_{\rm TC}$. Also by increasing the thermophoresis and Dufour parameters, the concentration boundary layer thickness increases, which results in an increase of the concentration profile. To investigate the magnetic field $h_{\rm x}$ in the axial direction and the current density J_z has allocation characteristics on $R_{\rm m}$ and M, we can observe from Figure 9(a) and (i) that the induced

magnetic field decreases as the Hartmann number increases. Due to the presence of the Lorentz force, it was found that the Hartmann number has a diminishing effect on the induced current density. The Lorentz force, a resistive force formed by the presence of magnetic flux, slows down the motion of fluid in the boundary layer. In addition, it should be noted that the behavior of the magnetic field (axial component) is significantly different from that of $R_{\rm m}$. Figure 9(a) shows the behavior of the current density distribution and we found that it gives a parabolic trend. Furthermore, as the value of $R_{\rm m}$ increases, the current density also varies. Figure 9(k) depicts the implications of temperature profiles for various N_t values. The temperature profile increases as the value of N_t increases, as seen in Figure 9. The mobility of the particles is due to the temperature gradient that exists in the external medium during thermophoresis. As a result, increasing the values of the thermophoresis parameter N_t increases the temperature of the fluids. This is because the temperature and N_t have a direct relationship.

Gradient values refer to the gradient values of the loss function with respect to the model's parameters during training. These values indicate how much the loss function changes as the model's parameters are updated, and can provide insights into how well the model is learning and whether adjustments need to be made to the learning rate or the optimization algorithm.

Epochs refer to the number of times the model has seen the entire training dataset during training. Increasing the number of epochs can improve the model's performance up to a certain point, after which overfitting may occur. The optimal number of epochs will depend on the size and complexity of the dataset and the specific model architecture being used.

Best training performance refers to the best results achieved by the model during training, usually measured by a performance metric such as accuracy or mean square error. This metric can be used to compare different models or variations of the same model and to evaluate the model's suitability for the intended application.

In terms of training and testing, one can see that a correlation with a value close to unity provides an ideal model, proving the validity of the suggested model ANN with the Levenberg-Marquardt technique for the peristaltic flow of a magneto couple stress fluid in a non-uniform channel. Table 2 shows the results from all the cases with different epochs.

The solution and error analysis curves are presented in Figure 9.

5 Conclusions

In this study, the peristaltic flow of a magneto couple stress fluid in a non-uniform channel is investigated subjected to the nanofluid flow system under the impact of convection through a double-diffusive system. In the presented fluid flow system, the mathematical formulations of magnetic properties of the nanofluid system are discussed and analyzed via intelligent computing infrastructure based on supervised learning. The outcomes of the study through the best representations of performance measures, histograms, and regression plots along with mean square error analysis are sources of reliance effectively. The axial-induced magnetic field as well as the temperature and concentration of nanoparticles are calculated to attain the outcomes of the presented study.

Some important findings are listed below:

- The solutal concentration and temperature distribution both increase.
- The concentration increases by increasing the values of the thermophoresis parameter N_t and the Dufour parameter N_{TC} This is because the concentration shows direct relation with $N_{\rm t}$ and $N_{\rm TC}$.
- The induced magnetic field (h_x) increases when $y \in [0,1]$, while it decreases when $y \in [1, 2]$.
- As compared to $R_{\rm m}$, the behavior of the axial magnetic field on *M* is the opposite.
- The behavior of the current density I_z increases with an increase in the values of $R_{\rm m}$.
- It is observed that increasing the values of N_t , the temperature profile (θ) increases.

New artificial intelligence-based computational intelligence networks will be designed in the future to successfully solve fluid mechanics constraints [43–45].

Acknowledgments: The authors extend their appreciation to the Deanship of Scientific Research at King Khalid University (KKU) for funding this research through the Research Group Program Under the Grant Number: R.G.P.2/451/44.

Funding information: The authors extend their appreciation to the Deanship of Scientific Research at King Khalid University (KKU) for funding this research through the Research Group Program Under the Grant Number: R.G.P.2/451/44.

Author contributions: All authors have accepted responsibility for the entire content of this manuscript and approved its submission.

Conflict of interest: The authors state no conflict of interest

References

- Latham TW. Fluid motion in peristaltic pump. Master's Thesis. Cambridge, MA, USA: MIT; 1966.
- [2] Shapiro AH, Jafferin MY, Weinberg SL. Peristaltic pumping with long wavelengths at low Reynolds number. J Fluid Mech. 1969:35:669.
- [3] Husseny SZA, Elmaboud YA, Mekheimer KS. The flow separation of peristaltic transport for maxwell fluid between two coaxial tubes. Abstr Appl Anal. 2014;2014:17. doi: 10.1155/2014/269151.
- [4] Bohme G, Friedrich R. Peristaltic flow of viscoelastic liquids. J Fluid Mech. 1983:128:109–22.
- [5] Brown TD, Hung TK. Computational and experimental investigation of two-dimensional nonlinear peristaltic flows. J Fluid Mech. 1977;83:249–72.
- [6] Hung TK, Brown TD. Solid-particle motion in two-dimensional peristaltic flows. | Fluid Mech. 1976;73:77–96.
- [7] Lykoodis PS, Roos R. The fluid mechanics of the ureter from a lubrication point of view. J Fluid Mech. 1970;43:661–74.
- [8] Shapiro AH, Jaffrin MY, Weinberg SL. Peristaltic pumping with long wavelengths at low Reynolds numbers. J Fluid Mech. 1969;37:799–825.
- [9] Taylor GI. Analysis of the swimming of microscopic organisms. Proc R Soc. 1951;209:447–61.
- [10] Kumar P. Magneto-rotatory thermal convection in couple-stress fluid. Int J Therm Fluid Sci. 2012;1(1):11–20.
- [11] Walicki E, Walicka A. Inertia effects in the squeeze film of a couplestress fluid in biological bearing. Appl Mech Eng. 1999;4:363–73.
- [12] Sharma RC, Sunil YD, Chandel RS. On couple-stress fluid permeated with suspended particles heated from below. Arch Mech. 2002;54:287–98.
- [13] Hayat T, Aziz A, Muhammad T, Ahmad B. Influence of magnetic field in three-dimensional flow of couple stress nanofluid over a nonlinearly stretching surface with convective condition. PLoS One. 2015;10(12):e145332.
- [14] Zhanga Y, Lib D, Cuib H, Yang J. A new modified model for the rheological properties of magnetorheological fluids based on different magnetic field. J Magn Magn Mater. 2020;500:166–377.
- [15] Zhu W. Iron nanoparticles-based magnetorheological fluid, A balance between MR effect and sedimentation stability. J Magn Magn Mater. 2019;491:165–556.
- [16] Kwon SH. Fe-Ga alloy based magnetorheological fluid and its viscoelastic characteristics. J Ind Eng Chem. 2020;82:433–8.
- [17] Rahim MSA, Ismail I. Review of magnetorheological fluids and nanofluids thermal behavior. Mater Sci Eng. 2015;100:012–40.
- [18] Tang X, Zhang X, Tao R, Rong Y. Structure-enhanced yield stress of magnetorheological fluids. J Appl Phys. 2000;87(5):2634–8.
- [19] Zhang XZ. Study on the mechanism of the squeeze-strengthen effect in magnetorheological fluids. J Appl Phys. 2004;96(4):2359–64.

- [20] See H. Field dependence of the response of a magnetorheological suspension under steady shear flow and squeezing flow. Rheol Acta. 2003;42:86–92.
- [21] Kulkarni P. Study of the behavior of MR fluids in squeeze, torsional and valve modes. J Intell Mater Syst Struct. 2003;14:99–104.
- [22] Prasad KV, Datti PS, Vajravelu K. MHD mixed convection flow over a permeable non-isothermal wedge. J King Saud Univ Sci. 2013:25(4):313–24.
- [23] Hasnain J, Abbas Z, Sajid M. Effects of porosity and mixed convection on MHD two phase fluid flow in an inclined channel. PLoS One. 2015;10(3):119913.
- [24] Yang M, Li X, Yuan J, Kang G. A comprehensive study on the effective thermal conductivity of random hybrid polymer composites. Int J Heat Mass Transf. 2022.;182:121–936.
- [25] Sharma S, Singh U, Katiyar VK. Magnetic field effect on flow parameters of blood along with magnetic particles in a cylindrical tube. J Magn Magn Mater. 2015;377:395–401.
- [26] Khan U, Ahmed N, Sikander W, Mohyud-Din ST. A study of velocity and temperature slip effects on flow of water based nanofluids in converging and diverging channels. Int J Appl Comput Math. 2015:1(4):569–87.
- [27] Khan U, Ahmed N, Mohyud-Din ST. Soret and Dufour effects on flow in converging and diverging channels with chemical reaction. Aerosp Sci Technol. 2016;49:135–43.
- [28] Bottemanne GA. Experimental results of pure and simultaneous heat and mass transfer by free convection about a vertical cylinder for Pr = 0.71 and Sc = 0.63. Appl Sci Res. 1972;25:372–82.
- [29] Chen TS, Yuh CF. Combined heat and mass transfer in natural convection along a vertical cylinder. Int J Heat Mass Transf. 1980;23:451–61.
- [30] Ellahi R, Rahman SU, Nadeem S. Blood flow of Jeffrey fluid in a catherized tapered artery with the suspension of nanoparticles. Phys Lett A. 2014;378(40):2973–80.
- [31] Waseem W, Sulaiman M, Kumam P, Shoaib M, Raja MAZ, Islam S. Investigation of singular ordinary differential equations by a neuroevolutionary approach. PLoS One. 2020;15(7):235–829.
- [32] Waseem W, Sulaiman M, Islam S, Kumam P, Nawaz R, Raja MAZ. A study of changes in temperature profile of porous fin model using cuckoo search algorithm. Alex Eng J. 2020;59(1):11–24.
- [33] Ahmad I, Ilyas H, Urooj A, Aslam MS, Shoaib M, Raja MAZ. Novel applications of intelligent computing paradigms for the analysis of nonlinear reactive transport model of the fluid in soft tissues and microvessels. Neural Comput Appl. 2019;31(12):9041–59.
- [34] Ahmad I, Raja MAZ, Ramos H, Bilal M, Shoaib M. Integrated neuroevolution-based computing solver for dynamics of nonlinear corneal shape model numerically. Neural Comput Appl. 2021;33(11):5753–69.
- [35] Patade J, Bhalekar S. Analytical solution of pantograph equation with incommensurate delay. Phys Sci Rev. 2017;2(9):20165103. doi: 10.1515/psr-2016-5103.
- [36] Liu Y. Numerical investigation of the pantograph equation. Appl Numer Math. 1997;24(2–3):309–17. doi: 10.1016/S0168-9274(97) 00028-7.
- [37] Rabiei K, Ordokhani Y. Solving fractional pantograph delay differential equations via fractional-order Boubaker polynomials. Eng Comput. 2019;35:1431–41. doi: 10.1007/s00366-018-0673-8.
- [38] Zahoor Raja MA, Shoaib M, El-Zahar ER, Hussain S, Li YM, Khan MI, et al. Heat transport in entropy-optimized flow of viscoelastic fluid due to Riga plate, analysis of artificial neural network. Waves Random Complex Media. 2021;1–20. doi: 10.1080/17455030.2022.2028933.

- [39] Aljohani JL, Alaidarous ES, Raja MAZ, Alhothuali MS, Shoaib M. Backpropagation of Levenberg Marquardt artificial neural networks for wire coating analysis in the bath of Sisko fluid. Ain Shams Eng J. 2021;12(4):4133–43.
- [40] Ilyas H, Ahmad I, Raja MAZ, Tahir MB, Shoaib M. Intelligent networks for crosswise stream nanofluidic model with Cu-H₂O over porous stretching medium. Int J Hydrog Energy. 2021:46(29):15322–36.
- [41] Tian W, Meng F, Liu L, Li Y, Wang F. Lifetime prediction for organic coating under alternating hydrostatic pressure by artificial neural network. Sci Rep. 2021;7(1):1–12.
- [42] Demirci F, Akan P, Kume T, Sisman AR, Erbayraktar Z, Sevinc S. Artificial neural network approach in laboratory test reporting: learning algorithms. Am J Clin Pathol. 2016:146(2):227–37.
- [43] Sabir Z, Imran A, Umar M, Zeb M, Shoaib M, Raja MAZ. A numerical approach for two-dimensional Sutterby fluid flow bounded at a stagnation point with an inclined magnetic field and thermal radiation impacts. Therm Sci. 2021;25(3):1975–87. doi: 10.2298/ TSCI191207186S.
- [44] Nagoor AH, Alaidarous ES, Sabir MT, Shoaib M, Raja MAZ. Numerical treatment for three-dimensional rotating flow of carbon nanotubes with Darcy–Forchheimer medium by the Lobatto IIIA technique. AIP Adv. 2020;10(2):025–16.
- [45] Ouyang C, Akhtar R, Raja MAZ, Touseef Sabir M, Awais M, Shoaib M. Numerical treatment with Lobatto IIIA technique for radiative flow of MHD hybrid nanofluid (Al2O3–Cu/H2O) over a convectively heated stretchable rotating disk with velocity slip effects. AIP Adv. 2020;10(5):055–122.
- [46] Shoaib M, Zubair G, Nisar. KS. Ohmic heating effects and entropy generation for nanofluidic system of Ree-Eyring fluid:

- Intelligent computing paradigm. Int Com Heat Mass Trans. 2021:129:105–683.
- [47] Raja MA, Shoaib M, Tabassum R, Khan MI, Gowda RJ. Intelligent computing for the dynamics of entropy optimized nanofluidic system under impacts of MHD along thick surface. Int J Mod Phys B. 2021;35(26):215–69.
- [48] Shoaib M, Zubair G, Nisar KS. Intelligent neuro-computing for entropy generated Darcy–Forchheimer mixed convective fluid flow. Math Comput Simul. 2022;201:193–214.
- [49] Prasannakumar BC. Heat and mass transfer analysis of radiative fluid flow under the influence of uniform horizontal magnetic field and thermophoretic particle deposition. Waves Random Complex Media. 2022;1–2. doi: 10.1080/17455030.2022. 2096943.
- [50] Afzal Q, Akram S, Ellahi R, Sadiq M, Chaudhry F, Thermal and concentration convection in nanofluids for peristaltic flow of magneto couple stress fluid in a non-uniform channel. J Therm Anal Calorim. 2021;144:2203–18. doi: 10.1007/s10973-020-10340-7.
- [51] Bhatti MM, Zeeshan A, Aleem Asif M, Ellahi R, Sait M. Non-uniform pumping flow model for the couple stress particle-fluid under magnetic effects. Chem Eng Commun. 2022;209:1058–69.
- [52] Zeeshan A, Riaz A, Alzahrani F. Eletroosmosis-modulated bio-flow of nanofluid through a rectangular peristaltic pump induced by complex traveling wave with zeta potential and heat source. Natl Library Med. 2021;42:2143–53.
- [53] Majeed A, Rifaqat S, Zeeshan A, Alhodaly MS, Majeed Noori F. Impact of velocity slip and radiative magnetized Casson nanofluid with chemical reaction towards a nonlinear stretching sheet: Three-stage Lobatto collocation scheme. Int J Mod Phys B. 2023;37(9):2350088.